Hyrcxwlrq#ri#hgjh#shghvwdo#wudqvsruw#ehwz hhq#hgjh0rfdol}hg#p rghv#q#GLLLG

J.-P. Floyd, W. M. Stacey, R. J. Groebner, and S. C. Mellard

Citation: Physics of Plasmas (1994-present) 55, 022508 (2015); doi: 10.1063/1.4907780
View online: http://dx.doi.org/10.1063/1.4907780
View Table of Contents: http://scitation.aip.org/content/aip/journal/pop/22/2?ver=pdfcov
Published by the AIP Publishing

Evolution of edge pedestal transport between edge-localized modes in DIII-D

J.-P. Floyd,[1] W. M. Stacey,[1] R. J. Groebner,[2] and S. C. McLeard[1]
[1]Georgia Institute of Technology, Atlanta, Georgia 30332, USA
[2]General Atomics, San Diego, California 92186, USA

(Received 25 October 2014; accepted 22 January 2015; published online 17 February 2015)

Evolution of measured profiles of densities, temperatures, and velocities in the edge pedestal region between successive ELM (edge-localized mode) events are analyzed and interpreted in terms of the constraints imposed by particle, momentum and energy balance in order to gain insights regarding the underlying evolution of transport processes in the edge pedestal between ELMs in a series of DIII-D [J. Luxon, Nucl. Fusion 42, 614 (2002)] discharges. The data from successive inter-ELM periods during an otherwise steady-state phase of the discharges were combined into a composite inter-ELM period for the purpose of increasing the number of data points in the analysis. Variation of diffusive and non-diffusive (pinch) particle, momentum, and energy transport over the inter-ELM period are interpreted using the GTEDGE code for discharges with plasma currents from 0.5 to 1.5 MA and inter-ELM periods from 50 to 220 ms. Diffusive transport is dominant for $q < 0.925$, while non-diffusive and diffusive transport are very large and nearly balancing in the sharp gradient region $0.925 < q < 1.0$. During the inter-ELM period, diffusive transport increases slightly more than non-diffusive transport, increasing total outward transport. Both diffusive and non-diffusive transport have a strong inverse correlation with plasma current. © 2015 AIP Publishing LLC. [http://dx.doi.org/10.1063/1.4907780]

I. INTRODUCTION

The edge pedestal is an important region of the plasma because there is experimental[1] and theoretical[2,3] evidence that overall plasma performance depends on the edge pedestal parameters. The sharp gradients found in the edge pedestal during high-confinement mode (H-mode)[4–6] operation are thought to be closely related to the increased confinement and performance of this operational regime.[7,8] These realizations prioritize the development of a more comprehensive understanding of the H-mode edge pedestal. The diffusive and non-diffusive transport mechanisms that determine edge pedestal structure and transport, and the thermodynamic and electromagnetic forces present in the edge, are subjects of ongoing research. For the full success of ITER and future devices, the cumulative results of these efforts must include a predictive capability for edge transport and profile structure which encompasses a broad range of operating regimes, plasma events, and reactor designs.

An unfortunate characteristic of normal H-mode operation is the cyclical occurrence of edge-localized modes[9] (ELMs), which can damage reactor components. Efforts to retain the high confinement and good performance of H-mode operation, while eliminating or mitigating the ELMs, have taken several different forms in recent years,[10,11] and high-performance operating regimes that do not feature ELMs have been developed.[12,13] The causes of Type I and other ELMs have been better understood through MHD peeling-ballooning theory,[14] but the transport processes involved in rebuilding the edge pedestal after an ELM to the point where another ELM can occur, are less thoroughly known. The present research seeks to understand edge transport during the rebuilding process, which reconstructs the sharp edge gradients after every ELM. A better understanding of the rebuilding process and its main drivers could contribute towards ELM mitigation or elimination efforts that focus on preventing the plasma from reaching a state where an ELM is likely to occur.

The purpose of the present research is to enhance the understanding of the edge pedestal, contribute to efforts to solve the ELM problem, and contribute to the development of a predictive capability for both. To this end, the measured evolution of plasma parameters between ELM events is interpreted in terms of the underlying evolution of diffusive and non-diffusive transport. Specifically, we interpret the transport from the evolution of measured density, temperature, rotation, etc., profiles, taking into account both non-diffusive effects (due to electromagnetic forces (particle pinch) and ion-orbit loss) and the requirements on the definition of the particle diffusion coefficient imposed by momentum balance, in order to identify those other transport effects that must be accounted for by neoclassical and turbulent transport, but we do not undertake a comparison with specific diffusive transport theories. (In this latter regard, we note the experimental evidence for instabilities present in the pedestal rebuilding[15,16] but do not further address this topic in this paper.) The present work is a broadly expanded follow-up to the one described in Ref. 17.

The ELMs linked to this research are successive, Type I (large, relatively low frequency, heating power dependent[9]) ELMs in H-mode on DIII-D, and the analysis is performed for four DIII-D shots with different plasma currents. Interpretation of this data is performed in the context of particle, momentum, and energy balance constraints on as fine a time scale as possible in order to facilitate the identification of inter-ELM evolution patterns. The measured plasma profile evolutions and variations thereof with current are presented in Sec. II, where the procedures for reducing the data

to a form amenable to analysis are also described. Section III discusses the interpretive methodology. The interpretation of diffusive and non-diffusive transport and heat transfer in these discharges is presented in Secs. IV and V. Conclusions are summarized in Sec. VI.

II. EXPERIMENTAL DATA FROM DIII-D DISCHARGES

A. Data selection, procedures, and organization

The four shots selected for analysis are all DIII-D[31] ELMing H-mode shots from the same set of experiments with plasma currents of 1.5, 1.2, 1.0, and 0.5 MA. The 1.5, 1.0, and 0.5 MA discharges were part of a current scan, being similar in other respects, while the 1.2 MA shot was the reference discharge for the scan, included to investigate if significantly different plasma geometry affects current dependence found among the other three discharges. In a right hand system, the positive toroidal direction is counter-clockwise when the tokamak is viewed from above, and the positive poloidal direction is downward at the outboard mid-plane. For these shots, the toroidal plasma current was positive, the toroidal magnetic field negative, and the neutral beam was in a co-current configuration.

Most of the important properties of the current scan shots were approximately equal, with a toroidal magnetic field of $B_t \approx -2.11$ T, a major radius of $R \approx 1.76$ m, a minor radius of $a \approx 0.59$ m, an elongation of $\kappa \approx 1.73$, a beam power $P_{beam} \approx 4.2$ MW, and a lower single null divertor configuration. The reference shot (1.2 MA) had a different geometry than the current scan discharges, with an elongation of $\kappa \approx 1.83$, different upper and lower triangularities, a larger volume, and the x-point located directly on the floor, rather than above it. These properties, along with a slightly lower toroidal field strength of $B_t \approx -2.06$ T and a few other minor differences, cause the reference shot (1.2 MA) data to be somewhat different from the current scan shots ($I_p \approx 0.5$, 1, and 1.5 MA).

This analysis used the established practice[18] of constructing a composite inter-ELM period from a set of successive inter-ELM periods, all occurring during the quasi-steady-state portion of an ELMing H-mode DIII-D discharge. The inter-ELM periods and quasi-steady-state intervals used to construct the composite period for each of the four shots are shown in Figure 1.

The fourth plot in Figure 1 clearly shows that the 0.5 MA shot included many ELMs exhibiting "dithering" behavior.[9] This is characterized by the presence of subsequent, smaller peaks occurring immediately after the large, initial peak in the divertor D_a signal which marks the ELM. The dithering behavior was not present in the higher-current shots, and in order to maximize similarity among the four composite inter-ELM periods being examined, it was decided to exclude from analysis those inter-ELM periods exhibiting this "dithering" behavior for the 0.5 MA shot. The inter-ELM periods in the quasi-steady-state period of the 0.5 MA shot that were included in the analysis are denoted by a "p" in Figure 1.

The ion data utilized in this research were gathered using the DIII-D CER/CXRS diagnostic system,[19] and the electron data were gathered using the DIII-D Thomson laser system.[20] The measured data from each inter-ELM period within the time selection (black rectangles in Figure 1) were combined into a composite inter-ELM period for each shot, and these composite inter-ELM periods were then partitioned into chronologically ordered fractions of the whole, hereafter referred to as intervals. Accounting for minimum data quantity requirements and a desire for narrow time intervals (for high time resolution), a minimum interval width was found for each shot. The minimum interval fractional width (of the composite inter-ELM period) for a shot was dependent on the number and length of the inter-ELM periods in the time selection for that shot.

The ELM event disrupts edge transport, breaks field lines, and transports large quantities of particles and heat to the chamber wall. This study examines the rebuilding of the edge pedestal and other parameters between these events, and excludes the phenomena that occur as a direct result of the ELM. In order to ensure the exclusion of transport directly associated with the ELM event, the divertor D_a signal (shown in Figure 1) was closely monitored for the large spikes in this measurement that are generally understood to mark the occurrence of an ELM. The first interval of the composite inter-ELM period for a shot was begun after the end of the longest of all of the leading ELM events in the time selection for that shot was complete. An example is illustrated in Figure 2.

The inter-ELM period parameters are summarized in Table I for each shot, including the minimum interval width

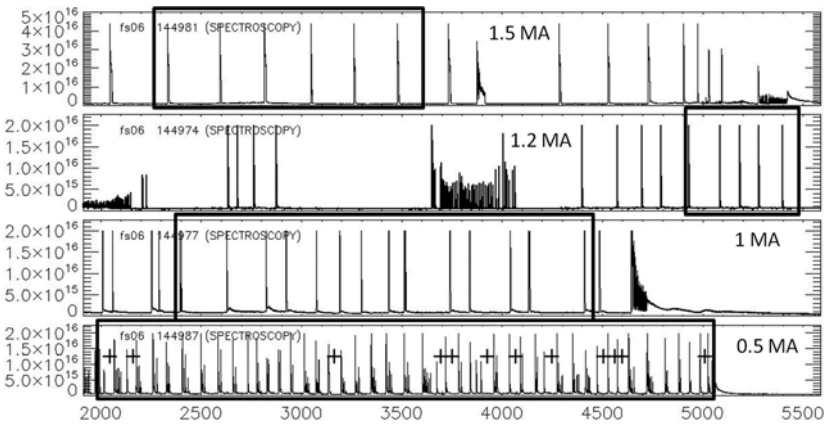

FIG. 1. The divertor D_a signal (photons/s) used to identify ELMs for the four shots between 2 and 5.5 s. The plots are arranged by current in decreasing order. The areas outside the time selection (denoted with a black rectangle) did not exhibit quasi-steady-state operation during the shot. The inter-ELM periods selected for analysis from the 0.5 MA shot quasi-steady-state period are denoted with a "p," and in the other shots, the entire set of consecutive, whole inter-ELM periods lying completely within the boxes were selected.

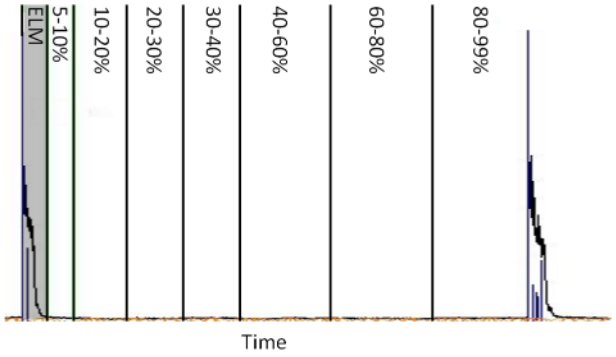

FIG. 2. A sample inter-ELM period for the 1.5 MA shot. The shaded area is considered to be part of the ELM event (0%–5% of the inter-ELM period). The first interval to the right of the ELM event is the minimum width for this shot (5%), and spans from 5% to 10% of the inter-ELM period. The subsequent intervals represent 10%–20%, 20%–30%, 30%–40%, 40%–60%, 60%–80%, and 80%–99% of the composite inter-ELM period.

and the longest leading ELM event duration. The minimum interval width (best time resolution) for a shot is directly related to the total length of time elapsing between ELMs in the time selection for that shot. Measurements show that plasma parameters change more rapidly early in the inter-ELM period; for the chronologically early intervals in the composite inter-ELM period, the minimum interval widths are used, while coarser time resolutions are used in the later intervals (usually a resolution of 20%, starting with the 40%–60% interval, as shown in Figure 2).

The intervals of the composite inter-ELM period for each of the shots are shown in Figure 3. The relationship between the fractional width (of the composite inter-ELM period for each shot) that an interval possesses, and the length of the same interval in absolute time, is displayed graphically. The location of the intervals from each shot and their widths, with respect to absolute time, in relation to those of the intervals of the other shots are also displayed. The 1.5 MA shot, in the uppermost position, has the longest average inter-ELM time of 220 ms for each shot, and therefore, its intervals collectively span the largest space. Due to space constraints and for clarity, only five intervals are shown for each of the four shots in most plots in the paper.

TABLE I. Characteristics of the selected ELMing H-mode DIII-D quasi-steady-state period from each shot. Percentages are the ratio of the interval width to the total composite inter-ELM period of the shot, and "best time resolution" in the text refers to the highest time resolution (minimum interval width) available for the composite inter-ELM period of each shot. The last column notes the end of the widest D_α spike of any leading ELM event in the selected inter-ELM periods for each shot.

Plasma current I_p	Average inter-ELM period	Number of inter-ELM periods	Minimum interval widths	Longest leading ELM event duration
0.5	54 ms	13 selected	17.5%	7.5%
1.0	156 ms	13	7.5%	7.5%
1.2	125 ms	4	10%	6.5%
1.5	220 ms	6	5%	5%

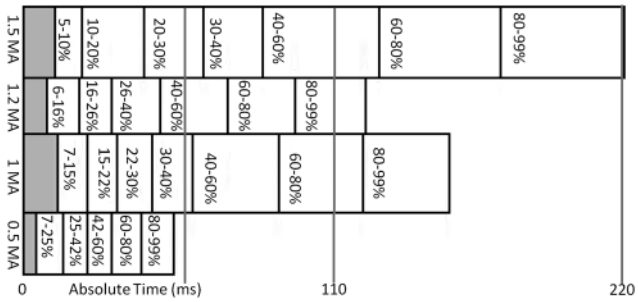

FIG. 3. The intervals of the composite inter-ELM period for each shot, shown in absolute time. The shaded area represents the length of the widest leading ELM event of the inter-ELM periods in the shot, while the black lines represent the end of the composite inter-ELM period for each shot. The continuous vertical lines in this plot are located at 0, 55, 110, and 220 ms in absolute time.

The short average inter-ELM period length (≤ 55 ms) for the 0.5 MA shot limited the length of the analysis period and the maximum time resolution for this shot. To counter these limitations, the location of the end of the longest leading ELM event was determined in a more aggressive manner, while still attempting to fully exclude it from the first interval. Consequently, for the first interval (7%–25%) of the 0.5 MA shot, there is a higher chance of the measured data being contaminated with ELM transport processes than for the first intervals of the other shots.

Once the intervals were created for each shot, data analysis scripts were used to facilitate the process of fitting profiles to the measured data contained in each interval. The script automatically fitted the electron data with "tanh" fits, which generally approximated the plentiful TS electron data trends well, and the ion data were fitted with spline fits. Due to a limited quantity of measured CER data available for these shots, the automatically generated spline profiles fitted to the ion data were less accurate, and had to be manually revised. These fitted, continuous profiles were sampled at twenty-five points in the plasma edge, starting in the flattop region at $q \approx 0.86$ and ending at the separatrix ($q = 1$). Other data necessary to simulate the experimental plasma were retrieved from the DIII-D MDSPlus database, and all the gathered data were compiled for input to the GTEDGE code,[21–23] which was used to interpret edge transport processes. Input to the interpretive GTEDGE code consists of the measured edge profiles of density, temperature, velocities, etc., plus experimental parameters such as confinement time, line average density, central density and temperature, radiation rates, impurity concentration, etc., that are used to characterize the background plasma. An emphasis was placed on maximizing the use of experimental data or values traditionally inferred from experiment (such as the radial electric field). The values of other quantities needed for the analysis (e.g., recycling neutral density) were calculated or interpreted from experimental data using GTEDGE. The equations used in GTEDGE for the interpretations are discussed later in the paper in conjunction with the results.

Once the plasma was simulated using GTEDGE, several model parameters were tuned to ensure the best possible match between the simulated background plasma and the

experimental plasma. The experimental parameters matched were the energy confinement time, line-averaged density, central density, central temperature, and plasma density and temperature at the top of the pedestal. These parameters were matched by adjusting corresponding quantities in the simulation, including the parabola-to-a-power shape of the density and temperature profiles, and the height of the temperature pedestal, then updating the simulation. This exercise was mostly done using an automated script developed for this purpose, but given the often nonlinear relationships between the pairs of quantities, the tuning process sometimes required complementary manual operation to be fully completed.

B. Experimental DIII-D data

The ion quantities measured with the CER system on DIII-D include the ion temperatures, densities and poloidal and toroidal rotation velocities,[19,24] while the Thomson laser system on DIII-D measures electron densities and temperatures.[20] The electron density profiles are shown in Figure 4, and display the familiar "edge pedestal" structure associated with H-mode operation. The structures of the electron density profiles at different radii will be labeled and used to refer to the corresponding area of the edge region throughout the paper. The "flattop region" is the inner part of the edge, where the density is relatively constant ($\rho < 0.95$ in the 1.5 MA shot). The "top of the pedestal" is the area where the densities begin to decrease ($0.95 < \rho < 0.97$ in the 1.5 MA shot), and the "sharp gradient region"/"pedestal" is the area between the flattop region and the separatrix ($\rho > 0.97$ in the 1.5 MA shot).

The electron density appears to increase monotonically in the flattop region as the pedestal is rebuilt, but the time difference between the profiles is not constant. In reality, the electron density pedestal height changes nonlinearly with time, increasing fastest immediately after an ELM, then gradually slowing as it approaches an asymptotic pre-ELM value (before the subsequent ELM, represented by the 80%–99% interval profile). This nonlinear evolution with time is seen in the evolutions of the other plasma profiles. The absolute maximum density seen in the edge for each shot is found at the end of the inter-ELM period, and the magnitude of this maximum increases as current increases.

Early in the inter-ELM period the density increases in the flattop region, but it actually decreases in the sharp gradient region. This evolutionary trend becomes more pronounced at lower currents. A very small decrease is found in the sharp gradient region for the 1.5 MA pedestal electron densities, but a decrease of nearly a third is found in the 0.5 MA shot at $\rho \approx 0.96$. The trend is also seen in the deuterium densities, and strongly implies the presence of inward transport for both particles between ELMs. During the inter-ELM period, the top of the pedestal increases in value and moves inward as it is rebuilt, sharpening the edge gradients, and widening the pedestal. The deuterium density profiles are similar to the electron density profiles, but with a lower magnitude due to the presence of impurities. They evolve in time and with current in similar ways.

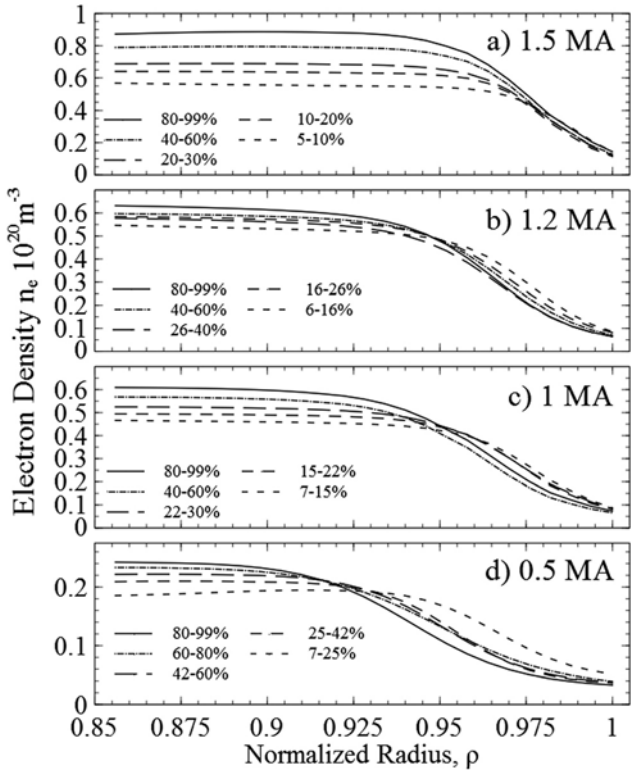

FIG. 4. The measured electron density profiles. For clarity, the Y axes differ in scale. For this plot, and most others in this document, the data from the earliest interval in the composite inter-ELM period, the interval immediately after the ELM, is represented by the trendline with the shortest dashes. As the end of the composite inter-ELM period approaches, the dashes become longer, and the density of the line becomes higher, with the 60%–80% interval being nearly solid. The last interval before the ELM, the 80%–99% slice, is represented by a solid line. This progression is clear in 4(a), above.

The impurity density fraction (f_z) generally decreases in the sharp gradient region, and increases inside of it throughout the inter-ELM period. This pattern is most clear in the highest current shot with the best confinement. Between ELMs, the impurity density shows similar trends to those seen in the electron density profiles, slightly decreasing in the sharp gradient region and increasing in the inner edge. As confinement decreases with decreasing current, the impurity density decreases nonlinearly, with the maximum flattop value dropping from ≈ 0.0375 in the 1.5 MA shot to ≈ 0.032 in the 1 MA shot to ≈ 0.0059 in the 0.5 MA shot.

The electron temperature profiles in Figure 5 also show a non-linear growth rate that is largest early in the rebuilding process, and have profile structures and evolutions similar to those of the electron density. However, there is no prominent decrease in temperature in the sharp gradient region. Also, no correlation between maximum temperatures and plasma current is apparent in the electron temperatures.

The ion temperature profiles are shown in Figure 6. The cliff-like pedestal shape of the electron density profiles is not found in the ion temperature profiles, where the "edge pedestal" is much less defined. Instead, the profile gradually decreases throughout the edge, with a slight change in slope indicating the presence of an ion temperature "pedestal" (e.g., $\rho \approx 0.91$ in the 1 MA shot).

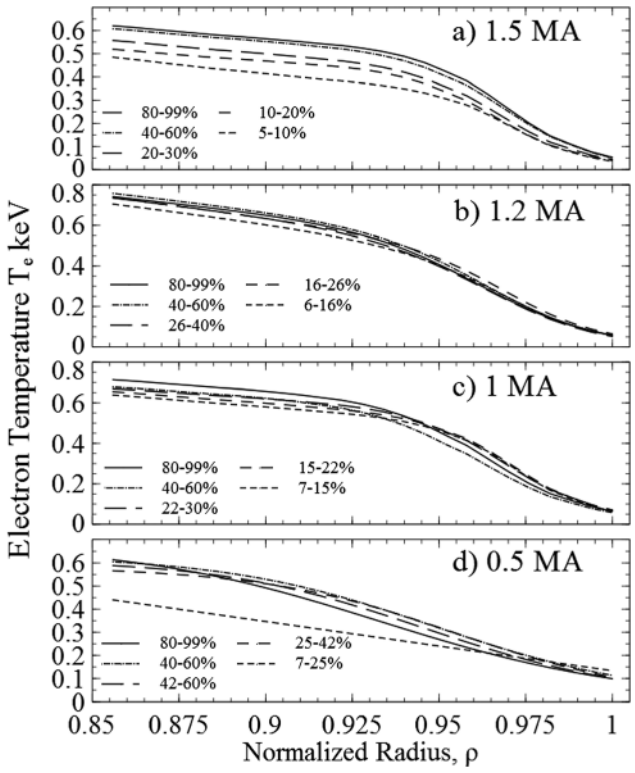

FIG. 5. The measured electron temperature profile evolution.

Between ELMs, the ion temperature rebuilds, and it does so in a way that varies with current. In the 1.5 MA shot, temperatures near the separatrix rise faster throughout the inter-ELM period than those further inward. However, in the 0.5 MA shot, the temperatures near the separatrix actually decrease in the first part of the shot, finally rising near the end of the inter-ELM period. The temperature rebuilding patterns in the 1.2 and 1 MA shots seem to lie between these two extremes, with a more consistent rebuilding pattern that still exhibits radial dependence. This variation in inter-ELM ion temperature rebuilding patterns is the main effect of changing current magnitudes on the ion temperature profiles.

The carbon poloidal rotation velocities for the four shots are shown in Figure 7. As discussed in Sec. IIA, a positive value in Figure 7 implies a downward velocity at the outboard midplane. The carbon poloidal rotation velocity profiles form a negative well in the sharp (density) gradient region, and the well generally decreases in width throughout the inter-ELM period. The characteristics of this well structure change substantially across the current scan. In the 1.5 MA shot, the minimum of the relatively shallow velocity well is around −7.5 km/s and deepens with decreasing current, reaching a well minimum of −20 km/s in the 0.5 MA shot, and developing steeper well walls.

These velocity evolutions exhibit a slight "overshoot" behavior, in which extreme profile values are reached midway between ELMs then relax somewhat towards the end of the inter-ELM period. This feature is well illustrated in all the plots in Figure 7, as the "asymptotic" pre-ELM (80% −99%) profile is rarely at an extreme. Similar overshoot behavior is found in the sharp gradient region of many other plasma parameter profiles examined in this analysis, such as the composite toroidal momentum transport frequency and the radial ion flux.

The carbon toroidal rotation velocity shown in Figure 8 decreases monotonically with radius throughout the edge. No clear trends in magnitude with current are found.

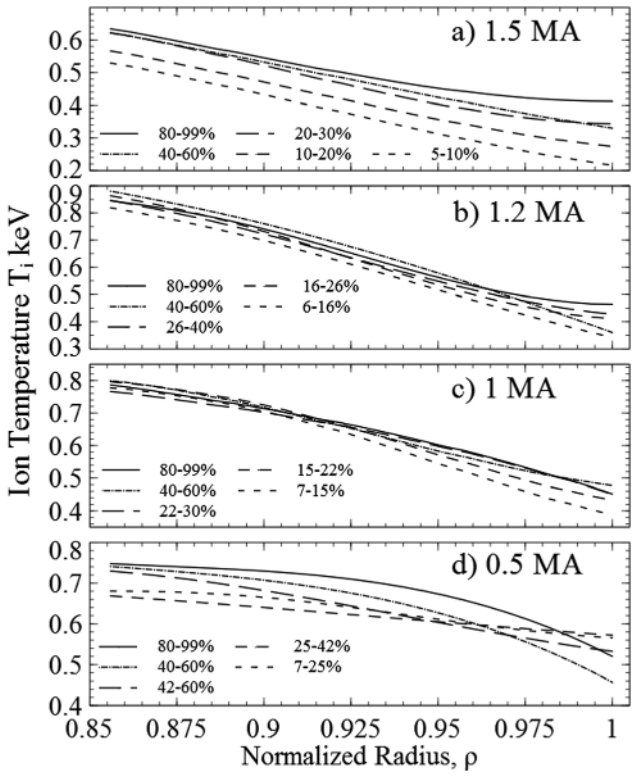

FIG. 6. The measured ion temperature profile evolution.

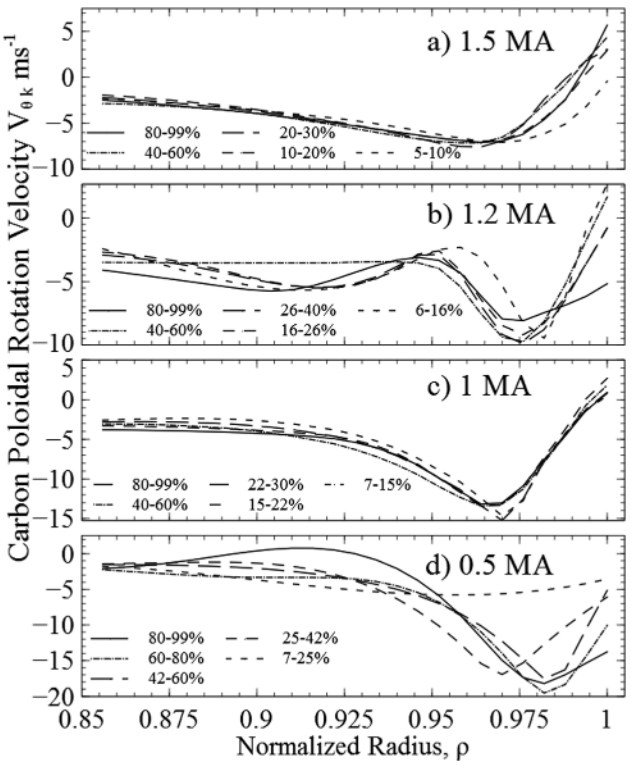

FIG. 7. The measured carbon poloidal rotation velocity profiles.

The CER-measured carbon density, temperature, and toroidal and poloidal rotation velocities are used (along with magnetic field strengths) to calculate the radial electric field[24] from the equilibrium carbon radial force balance equation

$$E_r^{exp} = \frac{1}{n_k^{meas} e_k}\frac{\partial p_k^{meas}}{\partial r} + B_\theta V_{\phi k}^{meas} - B_\phi V_{\theta k}^{meas}. \quad (1)$$

The radial electric field profiles for the four shots are shown in Figure 9.

The carbon poloidal rotation velocity has a strong influence on the values of the radial electric field. In the sharp gradient region, the pressure gradient term and the poloidal velocity term combine to create a negative well in the radial electric field. Generally, the well deepens throughout the inter-ELM period, and also exhibits considerable overshoot behavior in the sharp gradient region where the negative well is found.

As current magnitude changes, there are a number of trends that are detectable. The radial electric field becomes more negative across the edge with decreasing current, a trend caused by a larger pressure gradient term (due to smaller densities) and decreasing negative poloidal rotation velocity values. The width of the well also increases slightly with decreasing current, a result of the larger extent of the sharp gradient regions in the lower current shots. For example, from the 1.5 MA shot to the 1 MA shot, the width of the mouth of the E_r well for the pre-ELM 80%–99% interval increases about 25% from $\Delta\psi \approx 0.06$ to $\Delta\psi \approx 0.075$.

Typical error bars on the measured data are given and discussed in Ref. 17.

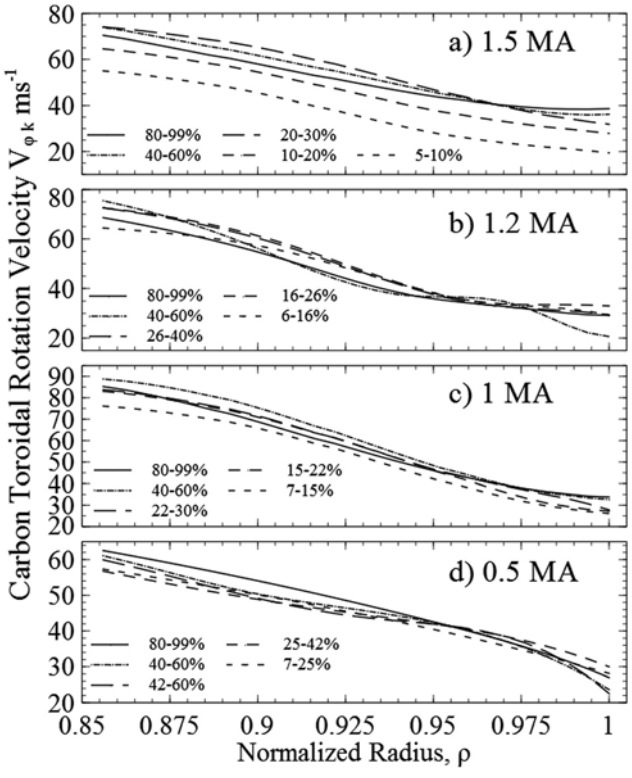

FIG. 8. Measured carbon toroidal rotation velocity.

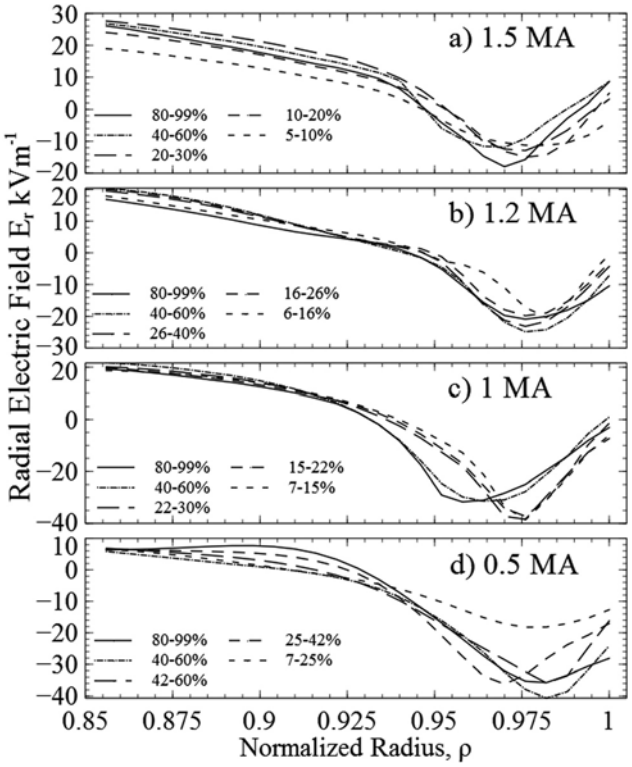

FIG. 9. Experimental radial electric field.

III. MOMENTUM AND PARTICLE BALANCE CONSTRAINTS ON PARTICLE TRANSPORT

In this section, we combine the toroidal and radial components of the momentum balance equation to derive a pinch-diffusion equation for the radial ion flux and to prescribe the diffusion coefficient and electromagnetic pinch velocity that are required by momentum balance. We also note that in the edge plasma, some of the more energetic thermalized ions can access orbits that exit the plasma, and instantaneously be lost from it. To take these losses into account, we present an ion orbit loss correction to the radial ion flux flowing in the plasma. In Sec. IV, we will use the data of Sec. II B to evaluate the particle diffusion theory and pinch velocities prescribed by momentum conservation, and calculate the diffusive and non-diffusive radial particle fluxes.

A. Radial ion particle transport

During the ELM event, there is a large flow of plasma in the edge directed radially outwards towards the first wall, much of which gets swept into the divertor. As the pedestal rebuilds immediately after the ELM event, oppositely directed inward flows of ions are necessary to replace the ions lost through the ELM and rebuild the pedestal structure. There are several fundamental transport mechanisms that are involved in this rebuilding of the edge pedestal throughout the inter-ELM period. For the ions, momentum conservation requires that the following forces remain in balance: (i) toroidal angular momentum exchange with other ions and neutral atoms via collisions, (ii) viscous and inertial torques exerted in the plasma due to ion bulk particle flows, (iii) electromagnetic ($V \times B$, electric field) forces, (iv) thermodynamic forces

(pressure gradient), and (v) external forces (e.g., momentum exchange with neutral beam particles). The loss of particles, energy, and momentum by ions that access unconfined trajectories, or loss orbits, and (nearly) instantaneously exit the plasma across the separatrix, must also be taken into account.

The collisional momentum exchange frequency between main deuterium plasma ions (denoted by subscript j) and the carbon impurity ions (subscript k) is represented by the collision frequency ν_{jk}, and can be calculated from measured data. In this paper, other types of toroidal momentum transfer in the radial direction, including charge exchange and the outward momentum flow due to viscous and inertial torques, are represented by the composite radial transport frequency of toroidal angular momentum, ν_{dj}. GTEDGE calculates neutral recycling using a coupled model of ion particle balance on the core plasma, a 2-point model for the ion flux to the divertor plate, and a 2D integral transport calculation of recycling neutrals into the plasma edge.[23] This composite frequency will be referred to as the drag frequency, and its magnitude will be interpreted from toroidal rotation measurements.[25] The electromagnetic $v \times B$ forces, the electrostatic E_r and E_ϕ forces, and the external beam momentum input $M_{\phi j}$ are represented explicitly in the ion momentum balance equation, the radial and toroidal components[26] of which are

$$V_{\phi j} = \frac{1}{B_\theta}\left(E_r + V_{\theta j}B_\phi - \frac{1}{n_j e_j}\frac{\partial p_j}{\partial r}\right); \tag{2}$$

$$B_\theta e_j C_{rj} = n_j m_j(\nu_{dj} + \nu_{jk})V_{\phi j} - n_j m_j \nu_{jk} V_{\phi k} - M_{\phi j} + n_j e_j E_\phi^A. \tag{3}$$

In these equations, V refers to particle fluid velocity, electric fields are denoted with an E and magnetic fields with a B. Density and charge are represented by n and e, and the momentum exchange (ν) frequencies have already been defined. Similar equations are obtained with the "k" and "j" subscripts interchanged for the impurity ion species.

The ion radial particle flux in the plasma exerts a torque that produces toroidal and poloidal flows of the plasma ions. For a two-species plasma model, the radial and toroidal momentum balance equation components (Eqs. (2) and (3)) can be solved[26] for the radial deuterium particle flux C_{rj}

$$C_{rj} = -\frac{n_j D_j}{p_j}\frac{\partial p_j}{\partial r} + n_j V_{rj}^{pinch} = -n_j D_j L_{pj}^{-1} + V_{rj}^{pinch};$$
$$L_{pj}^{-1} = \frac{dp_j/dr}{p_j}. \tag{4}$$

The collection of terms

$$D_j = \frac{m_j T_j \nu_{jk}}{(e_j B_\theta)^2}\left(1 + \frac{\nu_{dj}}{\nu_{jk}}\frac{e_j}{e_k}\right); \tag{5}$$

is a momentum-conserving definition of the diffusion coefficient. The second, non-diffusive term in Eq. (4) has a convective form, with the electromagnetic and external forces all collected in the "pinch velocity"

$$V_{rj}^{pinch} = -\frac{M_{\phi j}}{n_j e_j B_\theta} - \frac{E_\phi^A}{B_\theta} + \frac{m_j(\nu_{dj} + \nu_{jk})E_r}{e_j B_\theta^2} + \frac{m_j \nu_{jk} V_{\phi k}}{e_j B_\theta} + \frac{m_j(\nu_{dj} + \nu_{jk})V_{\theta j}B_\phi}{e_j B_\theta^2}. \tag{6}$$

The magnitude of the radial particle flux can be determined by solving the continuity equations (using the calculated recycling neutral source and neutral beam contributions)

$$\frac{\partial C_j}{\partial r} = -\frac{\partial n_j}{\partial t} + n_e n_0 \langle\sigma v\rangle_{ion} + S_{nb} = -\frac{\partial n_j}{\partial t} + S_{nj}. \tag{7}$$

The neutral beam source in this equation is denoted by S_{nb}, while the neutral ionization rate is given by the expression $n_e n_0 \langle\sigma v\rangle_{ion}$. The total source of deuterium ions is denoted with S_{nj}.

B. Ion orbit loss effects

Another important mechanism in edge transport is the instantaneous escape of ions that access loss orbits and immediately leave the plasma. This ion orbit loss (IOL) reduces the particles, energy, and momentum in the plasma; a return current of ions from the scrape-off layer (SOL) is required to balance the charge loss[27] and maintain macroscopic plasma neutrality. Both the ion orbit loss and the return current are taken into account using a numerical model,[28,29] which calculates the minimum energy required for a particle at a given location and with a given velocity to access a possible loss orbit and escape confinement. Using the conservation relations in Ref. 29, minimum escape energies [$\varepsilon_{min}(f_0) = 0.5 m V_{0,min}^2(f_0) = kT$] are calculated numerically, and expressions for the cumulative IOL-driven particle, momentum, and energy loss fractions in a given plasma at any radial location are evaluated

$$F_{orb} = \frac{\int_{-1}^{1} R_{loss}^{iol}\, C(3/2, \varepsilon_{min}(f_0))\, df_0}{2C(3/2)}; \tag{8}$$

$$M_{orb} = \frac{\int_{-1}^{1} R_{loss}^{iol}\, f_0 C(2, \varepsilon_{min}(f_0))\, df_0}{2C(2)}; \tag{9}$$

$$E_{orb} = \frac{\int_{-1}^{1} R_{loss}^{iol}\, C(5/2, \varepsilon_{min}(f_0))\, df_0}{2C(5/2)}. \tag{10}$$

Here, $F_{orb}(\psi)$, $M_{orb}(\psi)$, and $E_{orb}(\psi)$ are the radially cumulative loss fractions for ions, momentum, and energy, respectively, that escape across the separatrix, calculated from conservation of energy, magnetic moment, and canonical angular momentum.[29] The functions $C(n)$ and $C(n,x)$ are the gamma and incomplete gamma functions, respectively, while f_0 denotes the directional cosine of the particle velocity with respect to the magnetic field.

R_{loss}^{iol} is the fraction of particles crossing the separatrix that do not return into the plasma. There is ongoing work to define this fraction, and our best present estimate is that about half the ions leaving the plasma across the separatrix

are on orbits that return into the plasma. Thus, the assumption is made for this paper that one half of the particles calculated to leave the plasma do not return and are actually lost, $R_{loss}^{iol} = 0.5$. The cumulative fraction of total ions lost, F_{orbl}, at each radial location is shown in Figure 10 (with $R_{loss}^{iol} = 0.5$). These calculations take into account the measured variations of the radial electric field over the inter-ELM period and their effects on the ion orbit loss.

The cumulative ion orbit loss fraction is small except in the outer 5% of the plasma radius, where it increases rapidly to 30% –40% of the ions just inside the separatrix. The F_{orb} is inversely correlated with current, and changes very little with time over the inter-ELM interval. The energy loss E_{orb} variation is similar to that of F_{orb} shown in Figure 10.

The value for the radial ion flux derived from the continuity equation (Eq. (7)) must be reduced by the ions which escape confinement through IOL, and further reduced by the compensating inward current of ions necessary to maintain plasma neutrality[27]

$$\hat{C}_{rj}(r) = (1 - 2F_{orbl}(r))C_{rj}(r). \quad (11)$$

A quantity directly modified to account for IOL effects will be denoted with a carat. The radial ion flux profiles used in this analysis are calculated directly from the continuity equation and corrected for ion orbit loss, as indicated in Eq. (11). Figure 11 compares the calculated radial ion flux profiles just before and just after an ELM event for different values of R_{loss}^{iol}.

Figure 11 shows that a large fraction F_{orb} of the ions flowing radially outward in the plasma become free-streaming ions on orbits that escape the plasma in the outer radial few percent of the plasma. The loss fraction depends on the fraction R_{loss}^{iol} of the ions exiting across the separatrix which do not return inward across the separatrix to rejoin the ions flowing outward in the plasma. Since these free-streaming ion-orbit-loss ion are not being transported in the plasma, they should be subtracted from the total radial particle flux calculated from the continuity equation before that radial flux is used to interpret particle transport in the plasma edge. Similar corrections are needed for the outward flux of energy and momentum by ion-orbit-loss.

In the higher current shots, the IOL effect is concentrated near the separatrix, but as the current decreases, IOL becomes more substantial further inward in the sharp gradient region. This increased effect in the sharp gradient region as current decreases is shown in Figure 10, and is most prominent in the 0.5 MA shot. Taking the return current into account increases the influence of even small levels of ion orbit loss. The variations in the radial ion flux profiles with changing R_{loss}^{iol}, shown in Figure 11 for the 1 MA shot, are representative of the variations in the other shots.

Because ions are lost due to IOL, and because counter-current ions constitute a disproportionate share of the losses,[29] the momentum loss (Eq. (9)) due to IOL is preferentially counter-current, which causes an intrinsic co-current rotation in the edge plasma where IOL is high. An expression for the net parallel counter-current momentum loss rate due to IOL using the momentum loss rate (Eq. (9))[29] can be used to calculate the intrinsic co-rotation caused by IOL

$$V_{/j}^{intrin} = \frac{2}{p^{0.5}} M_{orbl,j}(q) \frac{2kT_j(q)}{m_j}. \quad (12)$$

A similar equation defines the intrinsic IOL rotation velocity associated with the carbon impurity by exchanging the "j" subscripts with "k" subscripts. Because of explicit mass dependence in Eq. (12), and the implicit mass dependence in M_{orb}, the intrinsic rotation velocity of carbon is nearly an order of magnitude smaller than for deuterium.

The momentum balance Eqs. (2) and (3), take collisional, viscous, inertial, external, and electromagnetic forces into account explicitly, but do not explicitly account for ion orbit loss of angular momentum. Components of these momentum balance equation are used to infer experimental

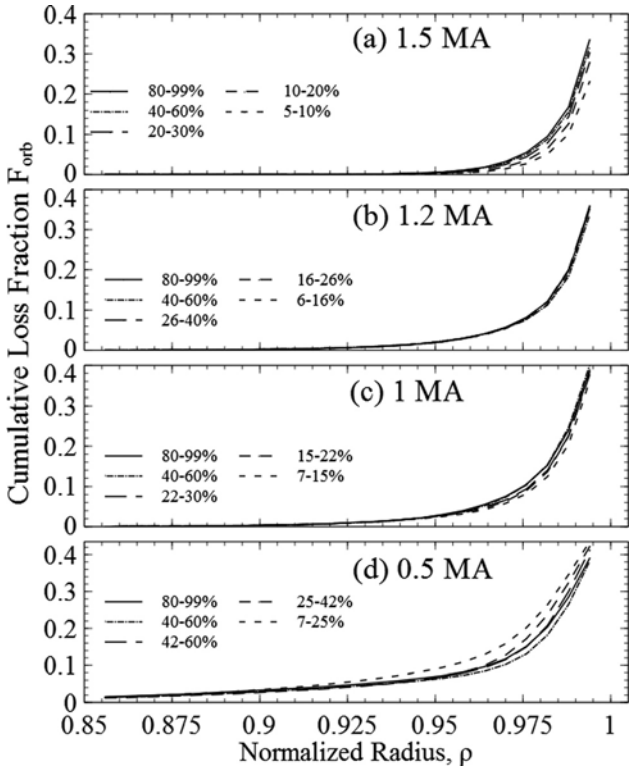

FIG. 10. The cumulative ion loss fraction as a function of radius with $R_{loss}^{iol} = 0.5$.

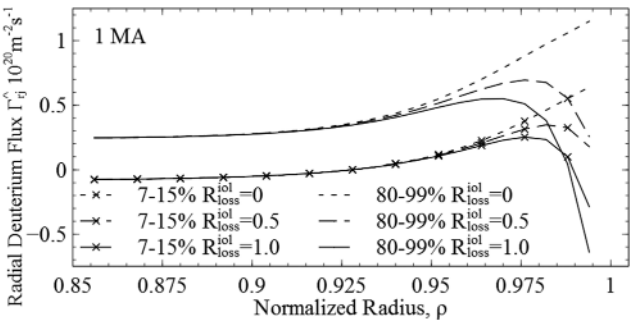

FIG. 11. Total radial ion flux just before (80% –99%) and just after (7% –15%, demarcated with "x") an ELM for the 1.0 MA shot, and for different values of R_{loss}^{iol}.

momentum transfer rates, which have a large influence on the interpretation of edge transport. For consistency, in the transport calculations utilizing the momentum balance equations, when "experimental" carbon and deuterium rotation velocities are either measured or constructed from experimental data, they must be corrected for IOL effects. To correct for IOL effects, the carbon toroidal intrinsic IOL rotation velocity is subtracted from the measured carbon toroidal rotation velocity.

$$\hat{V}_{/k} = V^{exp}_{/k} - V^{intrinsic}_{/k}. \quad (13)$$

Similarly, the deuterium intrinsic IOL toroidal rotation velocity $V^{intrin}_{/j}$ must be subtracted from the constructed deuterium toroidal velocity.

IV. RADIAL PARTICLE TRANSPORT INTERPRETATION

The experimental data presented in Sec. II are interpreted in this section in terms of the momentum and particle balance constraints of Sec. III. The deuterium radial particle fluxes calculated from the continuity equation and corrected for IOL are shown in Figure 12.

The outward radial ion fluxes peak in the sharp gradient region due to ionization of recycling neutrals, and decrease just inside of the separatrix because of ion orbit loss. Significant overshoot behavior is found in some of the shots. Aside from this, a general increase is seen during the inter-ELM period.

The radial ion flux values increase across the edge with lower current, the largest increase being in the sharp gradient region, and an inward shift of the sharp gradient region with lower current is also seen. This shift, and the increase in pedestal width that accompanies it, have been seen in several parameters, and will have a significant effect on the structure of the interpreted edge transport profiles.

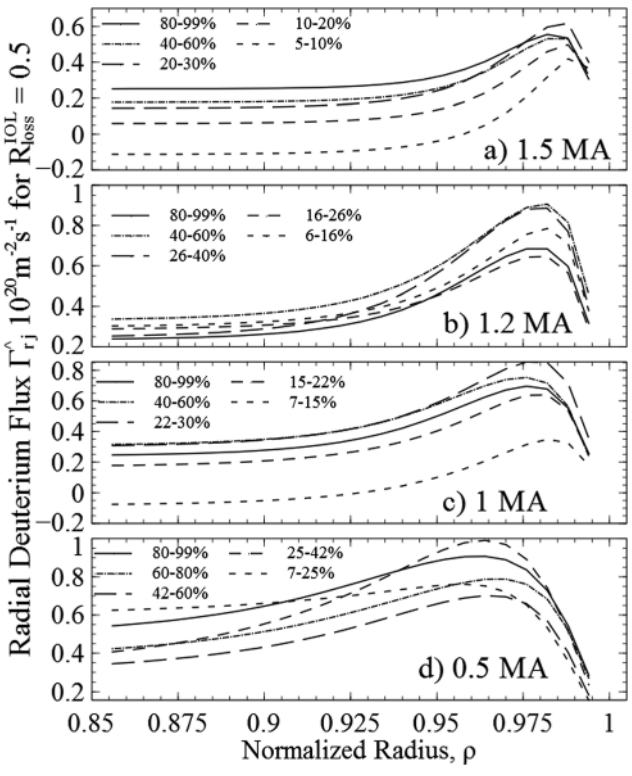

FIG. 12. The radial deuterium ion flux profiles accounting for IOL.

The radial ion flux profile of the first interval in each shot demonstrates interesting behavior, being negative and inward early in the 1.5 MA and 1 MA shot. The large Type I ELMs in these shots expel significant quantities of ions, which must be replaced to rebuild the density pedestal before the next ELM. This early influx of particles is largely a result of this mechanism. The flux profile for the first interval of the 0.5 MA shot may not reflect this influx for several reasons; two likely candidates are the lower time resolution available for this shot, or the possibility that the outward flux from the ELM event may still be influencing the flux in this interval, despite efforts to exclude it.

A. The diffusive particle flux

The total radial ion flux can be calculated from particle balance using the continuity equation, the known neutral beam source, and the calculated recycling neutral ionization source. As discussed, a fraction of the ion flux so calculated is in the form of free-streaming ion-orbit-loss particles, which must be compensated by an inward ion current, both of which reduce the ion flux actually being transported in the plasma. When this ion-orbit-loss correction is made, the remaining net ion flux in the plasma (shown in Figure 12) is described by the pinch-diffusion relation $\Gamma_{rj} = n_j D_j L_{pj}^{-1} + V^{pinch}_{rj}$ [Eq. (4)], where $D_j = \frac{m_j \Gamma_{jk}}{e_j B_h^2} \left(1 + \frac{\nu_{dj}}{\nu_{jk}} \frac{e_j}{e_k}\right)$ [Eq. (5)]. The diffusive flux is the first term of the pinch-diffusion relation: $\Gamma^{dif}_{rj} = n_j D_j L_{pj}^{-1} = n_j D_j (L_{nj}^{-1} + L_{Tj}^{-1})$. The quantity ν_{jk} is the deuterium-carbon collision frequency which can be calculated using the measured density and temperature. The quantity ν_{dj} is the deuterium toroidal angular momentum transport frequency due to viscous, inertial, charge-exchange and possibly other mechanisms. This is not presently known from first-principles but can be interpreted from the measured toroidal rotation velocities of both species, when they are measured. In this shot, only the carbon toroidal rotation velocity $V^{exp}_{/k}$ was measured, and it is necessary to use a perturbation estimate[25] of the difference between the carbon and deuterium toroidal velocities $\Delta V^{pert}_{/}$. The estimated deuterium toroidal rotation velocity $V^{pert}_{/j} = V^{exp}_{/k} - \Delta V^{pert}_{/}$ was then corrected for the calculated intrinsic rotation due to ion orbit loss[30] to obtain the IOL-corrected deuterium toroidal rotation velocity

$$\hat{V}_{/j} = V^{exp}_{/k} - \Delta V^{pert.}_{/} - V^{intrinsic}_{/j}. \quad (14)$$

In the perturbation method,[25] a leading order expression for the drag frequencies of both ion species is derived from toroidal momentum balance Eq. (3) using Eqs. (13), (14), and (11) to represent the carbon and deuterium corrected toroidal rotation velocities, and the corrected radial ion flux, respectively,

$$\nu_{dj} = \frac{\left[B_h e_j \hat{C}_{rj} \left(M_{/j} + n_j e_j E_/^A \right) + B_h e_k \hat{C}_{rk} \left(M_{/k} + n_k e_k E_/^A \right) \right]}{\left(n_j m_j + n_k m_k \right) \hat{V}_{/k}}. \quad (15)$$

The first order perturbation estimate of the difference between the deuterium and carbon rotation velocities can be obtained from Eq. (3) using perturbation theory

$$\Delta V_/^{pert:} = \frac{\left[B_h e_j \hat{C}_{rj} \left(M_{/j} + n_j e_j E_/^A \right) \right]}{\left(\frac{1}{2} n_j m_j \right) \left(\nu_{jk} + \nu_{dj} \right)}. \quad (16)$$

This provides an estimate of the drag frequency, ν_{dj}, and the velocity difference, $\Delta V_/^{pert:}$ which should be trustworthy when the deuterium toroidal rotation velocity is similar to that of carbon. The drag frequency profiles calculated using this method and the ion-impurity momentum transfer frequency ν_{jk} profiles are shown in Figure 13.

The structures of both of these profiles have a substantial impact on transport in the edge. During the inter-ELM period, the collisional frequency ($\sim n/T^{3/2}$) increases in the flattop region, but generally decreases in the sharp gradient region as confinement time increases. At all currents examined, the collisional frequency dominates the drag frequency throughout the inner edge, although the difference between the two narrows at lower currents.

Near the separatrix, the relationship between the two frequencies is strongly dependent on the value of the current.

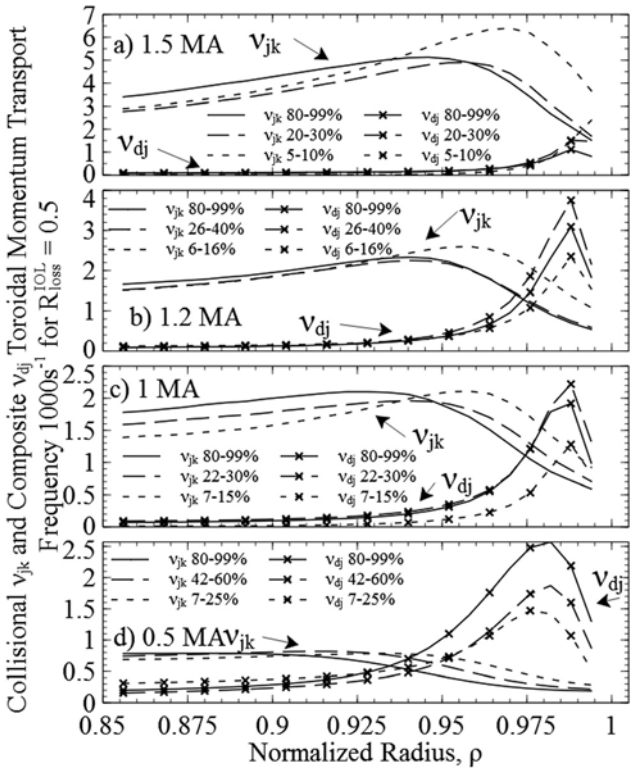

FIG. 13. The ion-impurity collisional toroidal momentum transfer frequency ν_{jk} and the composite toroidal momentum transport (drag) frequency ν_{dj} profiles evolve across the composite inter-ELM period. The drag frequency profiles are demarcated with "x."

The peak value of the collisional frequency is associated with the location of the top of the density pedestal. As the collisional frequency decreases and its peak moves inward with lower current, the drag frequency increases, and its peak also shifts inward.

The drag frequency becomes significantly larger than the collisional frequency near the separatrix in all but the 1.5 MA shot. The cause of this peak near the edge can be determined from Eq. (15), which is used to interpret the drag frequency from the carbon toroidal rotation velocity (Figure 8) and the radial ion flux (Figure 12). The drag frequency generally increases over the inter-ELM period in the sharp gradient region, but also exhibits overshoot behavior, which lessens at lower currents.

The corrected deuterium toroidal rotation velocities found from Eq. (14), and the deuterium toroidal IOL intrinsic rotation velocity calculated from Eq. (12) are shown in Figure 15. The corrected deuterium toroidal rotation velocity profiles decrease throughout the edge, and are influenced by the intrinsic rotation mainly near the separatrix. The intrinsic rotation velocity has similar inter-ELM evolutions and trends with current, and a related structure, to the loss fraction profiles in Figure 10. The deuterium toroidal rotation velocity profiles mirror many characteristics of the carbon toroidal rotation velocity profiles in Figure 8, justifying the use of the perturbation calculation. The main difference between the corrected carbon (not shown here) and corrected deuterium toroidal rotation velocity profiles are the presence of a larger intrinsic rotation velocity correction for deuterium. This is due to a larger cumulative momentum loss fraction M_{orb} from IOL for the deuterium species in the far edge, which causes a deeper depression near the separatrix. The broadening of the intrinsic rotation peaks with lower current is a structural feature also found in the drag frequency. In all cases, a contributor is the broadening area of IOL influence as current decreases, shown in Figure 10.

The deuterium diffusion coefficient of Eq. (4) that is required by momentum balance incorporates the ion composite momentum transfer frequency ν_{dj} (Figure 13, Eq. (15)) and the momentum exchange frequency ν_{jk} (also Figure 13) evaluated for the ion temperatures, as well as other variables. Figure 14 shows the deuterium diffusion coefficient evolution.

The deuterium diffusion coefficient strongly depends on the shape of the momentum transport frequency profiles shown in Figure 13, and their relative strengths. As the collisional momentum exchange frequency becomes less dominant at lower confinement and pressure (lower current), the peak deuterium diffusion coefficient value in the flattop region decreases accordingly. Also, as the drag frequency becomes larger in the sharp gradient region relative to the collisional frequency as current decreases, the diffusion coefficient profile more closely reflects the shape of the drag